

Rupture behavior of a moderate earthquake (M_W 5.9, April 2006) and its close relation with the 2003 Chengkung earthquake (M_W 6.8) at the southern termination of the plate boundary, southeast Taiwan



Laetitia Mozziconacci^{a,*}, Bor-Shouh Huang^a, Bertrand Delouis^b, Jian-Cheng Lee^a, Shiann-Jong Lee^a

^a Institute of Earth Sciences, Academia Sinica, No. 128, Section 2, Academia Road, Nangang, Taipei 11529, Taiwan

^b Géozaur, 250 rue Albert Einstein, Les Lucioles 1, Sophia Antipolis, 06560 Valbonne, France

ARTICLE INFO

Article history:

Received 7 February 2013

Received in revised form 8 July 2013

Accepted 15 July 2013

Available online 27 July 2013

Keywords:

2006 Taitung earthquake sequence

2003 Chengkung earthquake

Fault slip inversion

Fault geometry

Waveform inversion

Plate boundary

Earthquake initiation

ABSTRACT

The Taiwanese orogen is the result of the active and vigorous collision between the Eurasian and the Philippine Sea plates. In this strong convergence context, a one month-long earthquake sequence composed of two mainshocks of magnitude 6 occurred in April 2006 in the Taitung area. The first mainshock (T1) mobilized a structure just west to the plate boundary, while the second one (T2) is located on the other side. In order to retrieve the exact fault geometry of T2, we inverted waveforms from stations located at local and teleseismic distances. We performed a grid search on strike and dip (each strike-dip couple defining a geometry) considering the source as a point source then as an extended source. In the last case, a simple average over stations misfit failed to isolate a precise geometry. To overcome this problem, we used a more statistical approach on the distribution of misfits to define the best geometry. Comparing the best model to local structures, it appears the generative fault was the plate boundary that rotates from a strike pointing at N20°E north of the event to N0°E in T2 area with an identical eastward dip of 35°. For this model, the fault slip inversion provides a critical slip of 3.5 cm above which slip, rake and rupture time are constrained with uncertainties of 29%, 14° and 0.47 s respectively. The average slip along the rupture was 20 cm with a maximum of 46 ± 13 cm. The movement was inverse with a minor left-lateral component similar to the faulting behavior of the plate boundary. In addition, the slip pattern of T2 is contained within the southern portion of the deepest segment of the plate boundary and at the edge of the rupture area of the 2003 Chengkung earthquake (M_W 6.8), a large event also generated by the plate boundary but 2.5 years earlier. After 1 s of aseismic spreading, the rupture propagated seismically and circularly outward before being stopped by the fault bending.

© 2013 Elsevier Ltd. All rights reserved.

1. Introduction

Taiwan is an active orogen resulting from the collision between the Eurasian continental plate (EUP) and the Philippine Sea Plate (PSP). The onland plate junction is materialized by a narrow valley, the Longitudinal Valley (LV), filled with Quaternary sediments (Tsai et al., 1974). The valley is early defined as a suture zone between the two plates (Ho, 1986; Tsai, 1986) and lays between two mountain ranges: the Central Range (CER) to the West and the Coastal Range (COR) to the East (Fig. 1). The former belongs to the EUP while the later is part of the PSP. Previous studies on the LV indicate that this valley accommodates up to 25–30% of the total plate convergence (Angelier et al., 2000; Lee et al., 1998), explaining the intense seismicity of this region. More precisely, surface shortening occurs along structures on both sides

of the LV and parallel to it: the Longitudinal Valley Fault (LVF) to the east and the Central Range Fault (CRF) to the west (Fig. 1). However, those two structures are not equally active since the LVF is responsible for most of the deformation (geodetic and seismic) due to the collision and is therefore considered as the effective plate boundary (Angelier, 1984; Biq, 1972; Chai, 1972; Ho, 1982). On the other hand, the existence and the nature of the CRF is still a matter of debate because of its low activity and the absence of surface outcrop (Biq, 1965; Crespi, 1996; Lee et al., 2001, 2003; Malavieille et al., 2002). Despite the lack of evidences, Shyu et al. (2006, 2008) speculated that some minor shortening should take place on the CRF regarding the uplifted terraces that distribute along its supposed surface trace.

In April 2006, a one month-long seismic sequence occurred in the southern-end of the Longitudinal Valley, in the Taitung area. Its particularity is to contain two mainshocks of magnitude 6.0–6.1 separated by 14 days and about 20 km; each mainshock was followed by their respective aftershocks sequences. On April

* Corresponding author. Tel.: +886 2 2783 9910x407; fax: +886 2 2783 9871.

E-mail address: laetitia@earth.sinica.edu.tw (L. Mozziconacci).

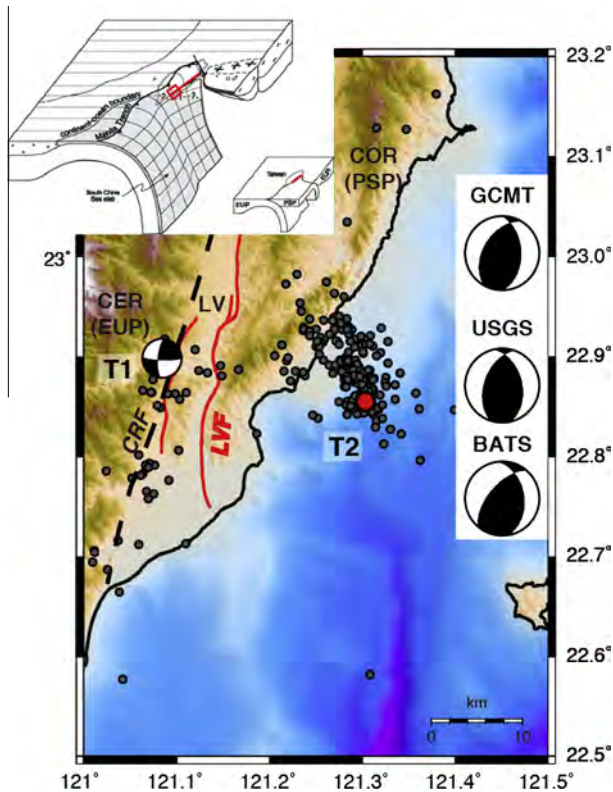


Fig. 1. Location of the two main large earthquakes of the 2006 April earthquakes sequence. Top left: 3D diagram of plate tectonics surrounding Taiwan (modified from Lallemand et al. (2001)). In gray is plotted the oceanic crust of the South China Sea (an oceanic crust that belongs to the Eurasian plate). Red line: Longitudinal Valley Fault. Red rectangle: study area. Main map: study area with the location of both earthquakes. The first event (labeled T1 on the Fig. 1) is plotted by its focal mechanism retrieved from Wu et al. (2006). The location of the second event (labeled T2) is indicated as a red circle. Only the sequence of aftershocks (gray shaded circles) of the second mainshock is plotted. Aftershocks are issued from the CWB and occurred up to 15 days after the mainshock. Events distribute along an alignment oblique to the Longitudinal Valley Fault (LVF). Next to the map, focal mechanisms of T2 are provided according to three different networks (BATS; GCMT; USGS). CER = Central Range. COR = Coastal Range. LV = Longitudinal Valley. LVF = Longitudinal Valley Fault. CRF = Central Range Fault. The LVF is indicated by red lines, while a dashed black line is used for the CRF since its surface trace remains uncertain. (For interpretation of the references to colour in this figure legend, the reader is referred to the web version of this article.)

1st 2006, the first mainshock (M_w 6.1) shook the western part of the southern portion of the Longitudinal Valley. Previous studies demonstrated that the CRF generated this event (Chen et al., 2009; Mozziconacci et al., 2013; Wu et al., 2006), bringing this earthquake as the first moderate-large event ever recorded for this structure since the installation of the Central Weather Bureau Seismic Network (CWBSN) in the late 1980s, and putting an end on the

Table 1

Location, magnitude and focal mechanism of T2 from different networks (BATS, CWB, GCMT, USGS). Planes refer to the two nodal planes (strike/dip/rake) of the focal mechanism. Networks are identical as those in Fig. 1.

Networks	Latitude	Longitude	Depth (km)	Magnitude	Planes: strike/dip/rake
CWB	22.856	121.304	17.9	M_L 6.00	
BATS	22.856	121.304	17.9	M_w 5.73	351/43/46 & 221/61/121
GCMT	22.870	121.400	21.7	M_w 5.90	258/48/66 & 212/47/115
USGS	22.802	121.362	08.0	M_w 5.90	246/46/65 & 200/50/114

debate on the existence of the CRF. Fourteen days later, on 15 April 2006, the second mainshock of the crisis (M_L 6.0), occurred off-shores, 10 km east of the Taiwanese coasts (Fig. 1). It is on this late event that we focus our study, and to simplify the reading we call it "T2" by comparison with the first event of the sequence ("T1" in the following text).

In the epicentral area of T2, the main local structure is the Longitudinal Valley Fault (LVF in Fig. 1), the effective plate boundary. It mainly strikes at $N0^\circ-20^\circ E$ and plunges eastward under the Coastal Range. The oblique collision between the EUP and the PSP results in the oblique movement on this structure, with a faulting 2/3 reverse and 1/3 left-lateral (Angelier et al., 1997; Barrier, 1985; Barrier and Angelier, 1986; Yu and Kuo, 2001). From the background seismicity a clear listric geometry was evidenced for the southern portion of the LVF; the dip varying from 60° to 70° in the first 10 km to less than 40° at deeper depth (Chen and Rau, 2002; Kuochen et al., 2004). Interestingly, three seismic networks (BATS, GCMT, USGS) give a consistent focal mechanism, mainly reverse in type with a small strike-slip component, compatible with the interseismic behavior of the LVF (Fig. 1 and Table 1). Concerning nodal planes of those focal mechanisms, all display one set oriented similarly to the LVF with north-south strike and a dip plunging eastward (Fig. 1). However, in map view, aftershocks of T2 align differently from the LVF strike or dip direction, rendering the link between this structure and the mainshock difficult to assume. To determine whether the LVF underwent the T2 earthquake, we performed a joint inversion of seismological data (from stations located at teleseismic and local distances) to retrieve the fault geometry and the fault distribution in space and time.

2. Data

We used two sets of seismological data from stations located at teleseismic and local distances from the epicenter. Local records are expected to be rather sensitive on the fault geometry and on the fault slip distribution in space and time. The use of teleseismic data allows a better azimuthal coverage and adds additional constrains on rupture timing.

2.1. Teleseismic data

From the IRIS data center, we selected 12 records of the P wave of stations located between 30° and 90° from the epicenter with a good azimuthal coverage (Fig. 2a). Since the earthquake is moderate (M_w 5.9 to 6.0, depending on the network, see Table 1), most of usable stations are located between 30° and 45° ; at further distances, records become too noisy to be exploited. After correction of the baseline, each record was deconvolved from instrument response and integrated in displacement according to the method of Nábělek (1984). A band-pass filter between 0.01 and 0.80 Hz and a time sampling of 0.25 s are used for an optimal time window of 30 s. Time windows are selected by trials and errors to contain direct waves and reflected phases and should be long enough to include any directivity effects.

2.2. Local strong motion data

We used 9 near-field local stations from the CWB network located between 9 and 95 km from the epicenter (Fig. 2b) and restricted within the PSP. The advantage of this restriction lays in a more homogeneous velocity model compared to the case of stations located on the two different plates that are the EUP (continental plate) and the PSP (oceanic plate). Station coverage is satisfying to the west of the epicenter with an epicentral distance lower than 30 km. However, to the east, the station on

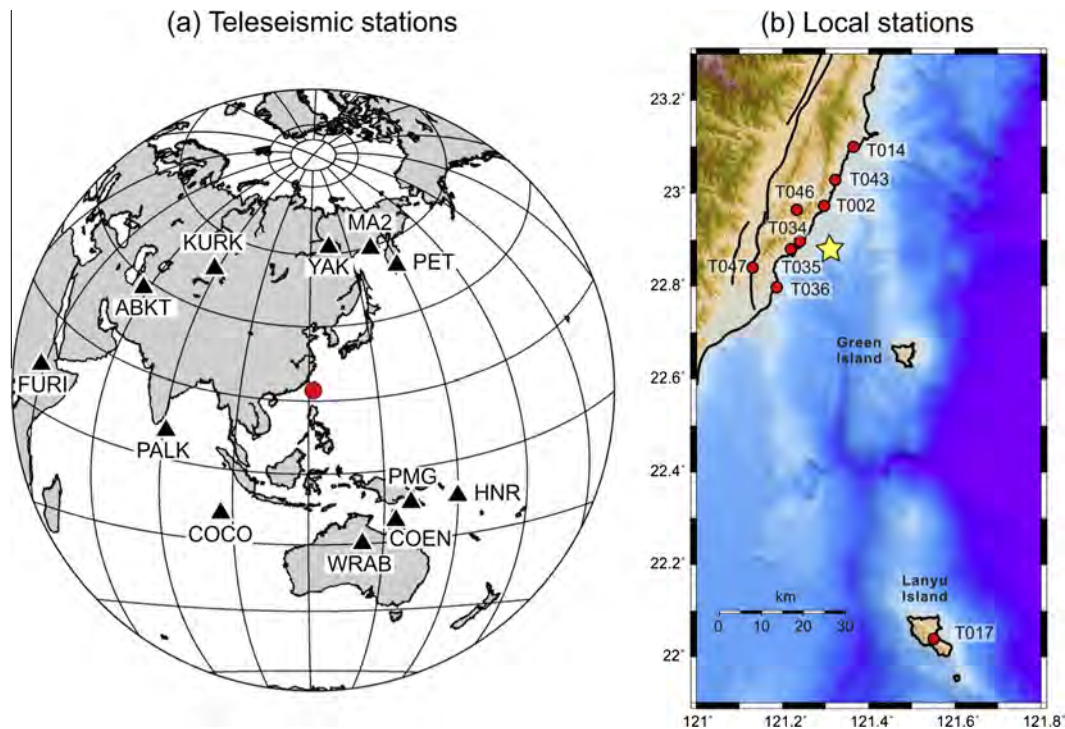


Fig. 2. Location of teleseismic and local strong motion stations. (a) Location of the 12 teleseismic stations. Black triangles indicate the location of stations. Red circle: epicenter of the T2 earthquake. (b) Location of the 9 local strong motion stations (red circles). Yellow star: epicenter of the earthquake. Name of islands located east of Taiwan are indicated in *italics*. (For interpretation of the references to colour in this figure legend, the reader is referred to the web version of this article.)

Green Island is too noisy to be used, and the coverage to the southeast can only be maintained by station T017 located on Lanyu Island (at 95 km from the epicenter). Similarly to teleseismic data, signal of local stations was integrated in displacement. An identical band-pass filter between 0.05 and 0.25 Hz and a time sampling of 0.5 s are used for all records. Contrary to teleseismic data, time window is retrieved from empirical relationships according to the method FMNEAR (Delouis et al., 2008; Delouis, submitted for publication). The time window is large enough to contain the near field and first surface wave arrivals (Delouis and Legrand, 1999; Delouis et al., 2008; Delouis, submitted for publication).

To determine the fault geometry of the structure that generated the T2 earthquake, we proceed in two steps. In a first step, we retrieved an average focal mechanism from a point source waveform inversion. At this point, we aim at establishing if both dataset converge toward an identical solution before to consider them jointly. In the second step, the source is taken as an extended source represented by a grid of point sources distributed on the fault. It is then possible to distinguish the fault plane from the auxiliary plane and test for its precise geometry.

Table 2

Input velocity model used for local strong motion. For each layer of the five models are indicated the P wave velocity (V_p) and the thickness (H). The ratio V_p on V_s (V_s for the S wave velocity) is 1.73. Models are listed with increasing number of layers from left to right, and abbreviations are done following this order: HS for half-space, 2C1 and 2C2 for the two two-layers models 1 and 2, 3C1 and 3C2 for the two three-layers models 1 and 2.

HS	2C1	2C2	3C1	3C2					
H	V_p								
∞	6.1	5	4.0	5	5.0	3	2.0	3	3.0
		∞	6.0	∞	8.0	3	4.0	3	5.0
						∞	6.0	∞	8.0

3. Focal mechanism

3.1. Method

3.1.1. Local strong motion

With local strong motion data, focal mechanisms are determined with the method FMNEAR (Delouis et al., 2008; Delouis, submitted for publication). This method is composed of two main steps. In the first one, we performed a coarse grid search on the strike and dip, and made the rake inverted. In the second step, results obtained in the first one are refined. Each geometry tested by the grid search (i.e. each strike-dip couple) is associated to a best rake and a waveform adjustment misfit. The misfit is quantified by the difference between observed and computed waveform and is low for good adjustment. More exactly, the expression of the misfit (rms) is the sum of two functions, the first one corresponding to the L2 norm fitting function of observed and computed waveforms, and the second one to the seismic moment minimization in a similar expression as Eq. (3) (Section 5.1). The rake is obtained by a simulated annealing algorithm used to minimize the waveform misfit (Delouis et al., 2002; Ihlmlé and Ruegg, 1997; Kirkpatrick et al., 1983). Synthetic waveforms are computed using the discrete wavenumber of Bouchon (1981) in a layered structure. We took advantage of the fast computation time of this method to determine a specific 1D velocity model for each station.

As mentioned above, the selected near-field local stations are exclusively located on the PSP (an oceanic plate) in order to profit from a more homogeneous medium than if stations were located on different kind of plates (the EUP being a continental plate). However, difference in local structures may exist from one station to another, and those lateral variations can be considered in using a specific 1D velocity model by station. To determine those models, we first retrieve focal mechanism using a half-space as velocity structure for all stations (Table 2). We obtained the following mechanism: strike = N350°E, dip = 30° and rake = +047°. We kept

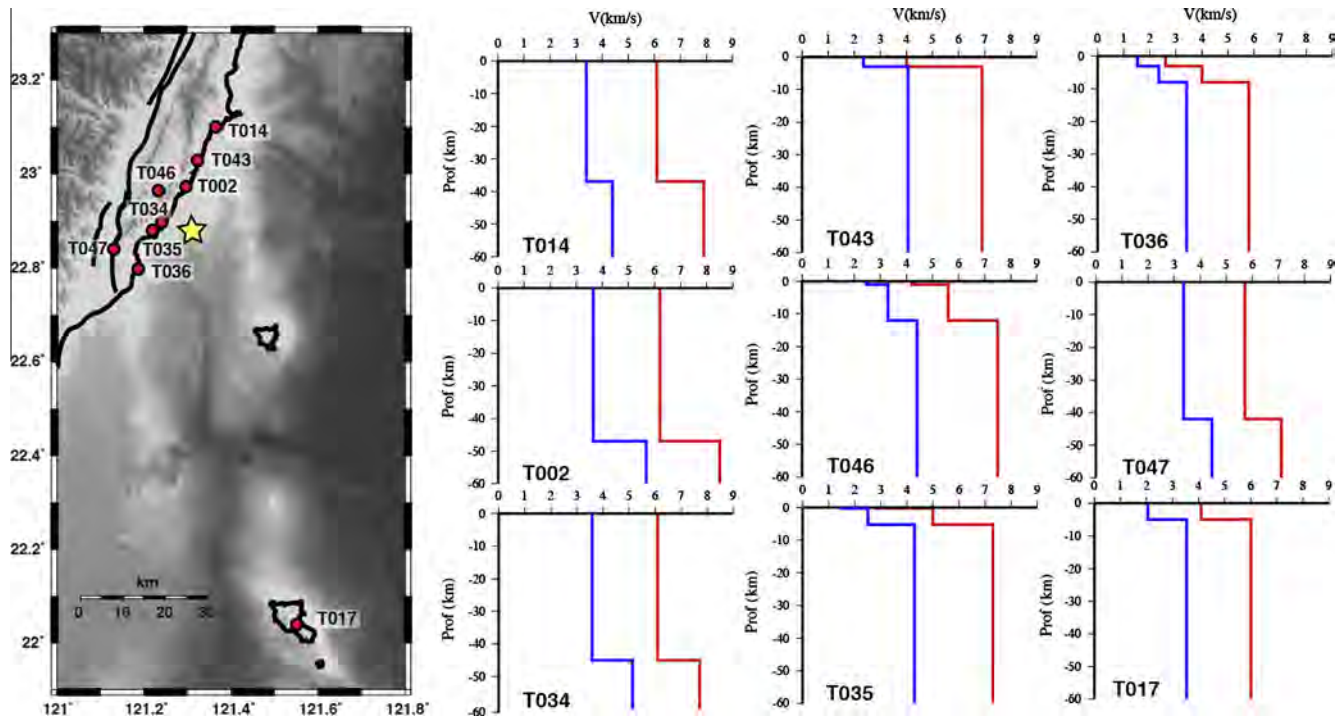


Fig. 3. Velocity models for each local strong motion station. 1D velocity models are plotted as graph where depth (in km) is function of the velocity (in km/s). Red lines: V_p . Blue lines: V_s . On the map, stations are plotted by red circles and the epicenter of T2 by a yellow star. (For interpretation of the references to colour in this figure legend, the reader is referred to the web version of this article.)

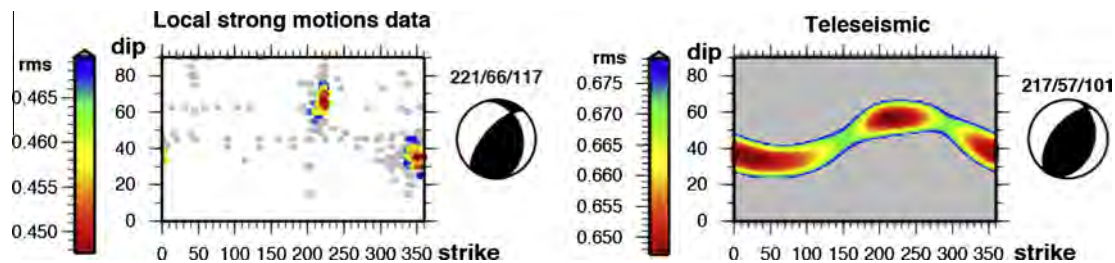


Fig. 4. Results of the grid search on the two kinds of data (local and teleseismic). Graphs of dip as a function of strike indicate the number of possible geometries. Color scale depends on the misfit between observed and computed waveform (rms) for the best 5% of the solutions. Gray solutions are for geometries with rms larger than 5% of the best one. Next to each graph is plotted the focal mechanism of the best solution, with above parameters of one of the two nodal planes.

fixed this mechanism while processing velocity model. In details, we processed the model of one station while the others remain with the half-space model. This processing is done by minimizing the rms in adjusting the velocity of the P wave (V_p), the ratio V_p on V_s (V_s for the S wave velocity) and the thickness of each layer as we previously done for the T1 earthquake (Mozziconacci et al., 2013). Since the result is dependent on the input model, we used five different starting models listed in Table 2 with increasing number of layers. From the five optimized models, we selected the one that provides the best waveform adjustment as final 1D layered velocity model.

The resulting velocity models are plotted in Fig. 3. Five local stations out of nine (T043, T036, T035, T046 and T017) need an uppermost layer of low velocity corresponding to shallow sedimentary layers while the remaining four stations can be modeled with a more simple velocity structure (half-space). We checked that layers thickness of 1D velocity models are well resolved by our data according to the band-pass filter we used on the records.

Focal mechanism determination with 1D velocity models compared to half-space (Fig. R 1) display results with less dispersion around the best one and a better waveform adjustment. The best

result of the grid search with layered velocity models (Fig. 4 and Fig. R 1) is similar to the first determination (350/30/+047 for half-spaces compared to 340/36/+044 for layered models). This similarity indicates that velocity models were computed with a focal mechanism suitable for the T2 earthquake implying that the resulting models correspond to stations site and path effects. In other words, the focal mechanism determined with 1D velocity models is corrected from those effects.

3.1.2. Teleseismic data

We determined focal mechanism parameters (strike, dip and rake) by a similar method as FMNEAR but adapted to teleseismic waveforms. Since Green's function of teleseismic data are less time consuming, we performed a grid search on strike and dip every 2° while we inverted the rake following the method of Nábělek (1984). As for local strong motion, each geometry is associated to a best rake and a misfit between observed and computed waveforms (rms). At teleseismic distances, we use the ray theory approximation of Nábělek (1984) to compute synthetics with a point source, 26 triangle source time functions of half duration 0.6 s and a half space velocity model. The half space is character-

ized by velocities on P and S waves of 6.00 and 3.46 km/s respectively and a density of 2.50 g/cm³.

3.2. Results

The results for both the local and teleseismic data are plotted on a graph where the dip is revealed as a function of the strike (Fig. 4). On all strike-dip graphs used in this paper, the best solution is the minimum rms of the color scale (in red). Only solutions at less than 5% in term of rms (the rms at 5% being the maximum rms of the color scale, in blue) are plotted with circles with colors corresponding to the color scale defined above (from red to blue), while solutions at more than 5% are plotted with gray circles.

Local and teleseismic data display strong similarities on their results. Both of them converge toward two nodal planes of a very similar focal mechanism indicating the two data sets are compatible for a joint inversion. Between the two sets of data, a better convergence is obtained with local strong motion records. This difference is likely due to the mainshock magnitude that is not high enough to be better constrained by teleseismic data. However, the similarity of solutions found by the two data sets (strike/dip/rake = 211/66/+117 and 340/36/+044 for local strong motions compared to 215/57/+101 and 017/35/+074 for teleseismic records) implies that the fault involved with the T2 earthquake is striking in the north–south direction and dipping either gently eastward or more steeply westward with an average movement nearly pure reverse.

In order to determine which plane is the fault plane amongst the two nodal planes, and since both data sets are compatible we performed a joint inversion of the two data sets by considering the source as an extended source where an array of point sources is distributed along a fixed geometry.

4. Test of the fault geometry

During the point source inversion of focal mechanism, we determined two sets of possible geometries corresponding to the two nodal planes of the same reverse focal mechanism. Both sets strike north–south and the difference between them lays in their dip direction. To avoid any confusion between them, we simplify the notation by *PE* for the east dipping plane and *PW* for the plane plunging westward.

As we mentioned before, both data sets are compatible to model the T2 earthquake even if teleseismic data provide a larger dispersion than local data on strike and dip values (Fig. 4). In order to constrain the fault plane geometry, we jointly inverted local and teleseismic data by a similar approach as for the focal mechanism determination except that we used an extended source.

4.1. Extended source inversion

The coseismic fault slip distribution is computed from the method of Delouis et al. (2002), where the source is an array of point sources that distributes inside one or several rectangular fault plane segments. The coseismic fault slip variation in space and time is retrieved by a simulated annealing algorithm (Ihmlé and Ruegg, 1997; Kirkpatrick et al., 1983; Lundgren et al., 1999) associated to a time window formulation (Olson and Aspel, 1982). The advantage of this algorithm is its ability to resolve non-linear problems without being dependent on a starting model. However, it does require *a priori* bounding values for free parameters (Delouis et al., 2002).

Fault plane dimensions are retrieved from the rupture length (9 km) estimated from the moment magnitude (Wells and Coppersmith, 1994). In order to avoid any border effects, rupture

dimensions are defined to be larger than two times the estimated rupture length (for a square model). For T2, we used a square fault plane of 22 km in length that we subdivided in 121 square sub-faults of 2 km length. For each sub-fault, the rake, the height of one time window (moment rate triangular function) and the time delay of the rupture front are inverted. The rake is allowed to vary 50° around an average value that was previously determined during the focal mechanism inversion with a point source. Subfault slip is linked to the time window area. Finally, the time delay of the triangle is adjusted within a time range defined by two bounding rupture velocities of 1.0 and 3.4 km/s. By a grid search on the number of triangles and their half duration we determined that one triangle of 0.5 s half duration allows the best waveform adjustment. The convergence of the algorithm is based on the minimization of the misfit between observed and computed waveform, a smoothing function on the slip distribution and a minimizing function of the total moment release (Delouis et al., 2002). The sum of

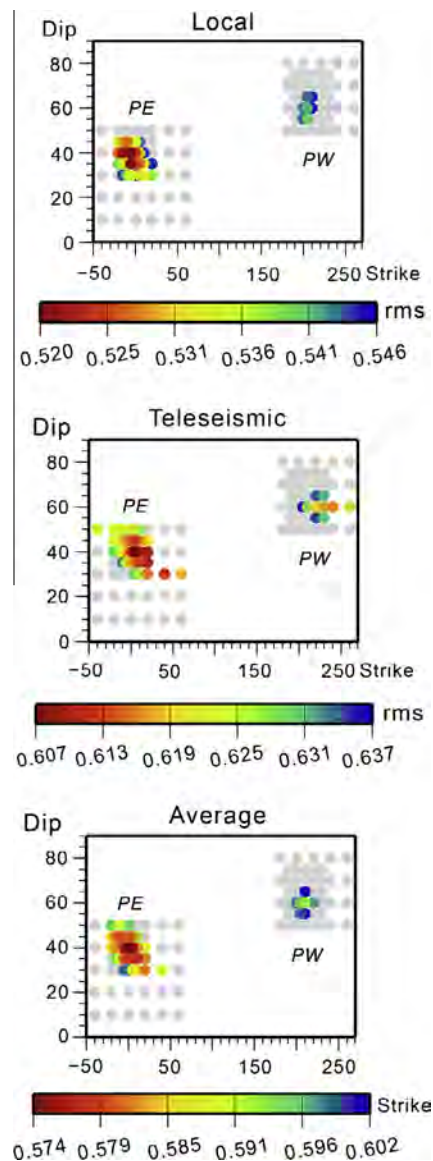


Fig. 5. Results of the grid search in graphs of dip as a function of strike. Each graph corresponds to one kind of data (local data to the left and teleseismic data to the center) to compare with the waveform average over the two datasets (to the right). Colored circles correspond to solutions that deteriorate the best waveform adjustment less than 5%, otherwise solutions are plotted in gray. *PE* and *PW* refer to the two sets of plane (see text).

those three functions will be referred as rms as in focal mechanism determination (paragraph 3). We use the same abbreviation (rms) because the difference between focal mechanism determination and fault slip inversion in the expression of the rms is the smoothing function on the slip that is null for the focal mechanism part.

4.2. Grid search

We performed a grid search on strike and dip in three steps, the grid being centered on the best result of the previous step. For each geometry tested is computed the fault slip distribution in space and time by minimizing the misfit between observed and computed waveform (rms) as explained in the Paragraph 4.1. In the grid search, the first step testes strike every 20° and dip every 10°. Then, the mesh is reduced to 10° (strike) and 5° (dip), before being reduced again to 5° (strike and dip) in the last step.

We tested *PE* and *PW* independently. For *PE*, strike is tested from N320°E to N060°E through N000°E, and dip between 10° and 50° for a rake of $55 \pm 50^\circ$. For *PW*, strike is tested between N180°E and N260°E, and dip between 50° and 80° for a rake of $100 \pm 50^\circ$. In order to have a continuous scale on strike for the set *PE*, we subtracted 360° to strikes larger than 180°. Results on the grid search are displayed in Fig. 5 in graphs of the dip as function of strike. Only solutions that deteriorate the best waveform adjustment (in term of rms) less than 5% are displayed with colored circles. It clearly appears that the fault plane of the T2 earthquake is in the *PE* domain, however, its precise geometry remains unclear with this approach. If we look at detailed results for each station (Figs. R 2 and R 3), best results highly vary from one station to another. If a station strongly converges toward a result that other stations reject, the contradictory station will bias the average result. However, no station can be removed *a priori* from the computation since no geometry is clearly favored by a majority of stations (Figs. R 2 and R 3).

To solve the problem on the identification of a clear fault geometry, we adopt a more statistical approach on the distribution of misfit between improvement and deterioration induced by one model compared to all geometries tested.

4.3. Statistical selection of the best geometry

Rather than choosing the fault geometry from the average waveform misfits, we compare relative waveform adjustment provided by models. To simplify the reading, we call model each geometry (strike-dip couple) for which a slip distribution and a waveform misfit (in term of rms) was computed. This approach is based on the difference in improvement/deterioration of the misfit (rms) provided by one model (taken as reference) compared to all the remaining tested models. Graphs with station misfits of all models (rms_{Mtot}) as function of station misfits of the tested model (rms_{Mtest} , Fig. 6) provide a qualitative view of this comparison. In these graphs, each station contributes for $(g - 1)$ misfits, g being the number of models that have been considered in the grid search. If the tested model improves waveform adjustment (compared to other models), misfits of other models will be larger than the tested one and will distribute mainly above the line of equal rms ($rms_{Mtot} = rms_{Mtest}$, Fig. 6).

To quantify the relative misfit improvement of one model compared to all the remaining ones, we estimate the repartition of misfits on both sides of the line of equal rms. This repartition does not display a pure Gaussian shape (Fig. 6) but is affected by some skewness. We have tested this tendency in our approach but the use of the mode (that is strongly dependent on the number of bins of a histogram) rather than the mean lead to imprecise results on the fault geometry (Figs. R 4 and R 5). As a consequence, this repartition can be simplified as a Gaussian distribution (Fig. 6), and the quantitative estimation of the improvement/deterioration of a model can be retrieved by computing the Gaussian curve parameters (μ and σ^2) of the repartition:

$$f(x) = \frac{1}{\sqrt{2\pi\sigma^2}} e^{-\frac{(dms-\mu)^2}{2\sigma^2}} \quad (1)$$

dms is the misfit difference between the tested model and the remaining ones ($dms = rms_{Mtot} - rms_{Mtest}$), μ , the mean of the repartition and σ^2 , the variance of the repartition ($\sigma^2 = \frac{1}{g-1} \sum_1^g (dms - \mu)^2$). As σ^2 also symbolizes the width of the Gaussian curve, a good result will provide a Gaussian curve with

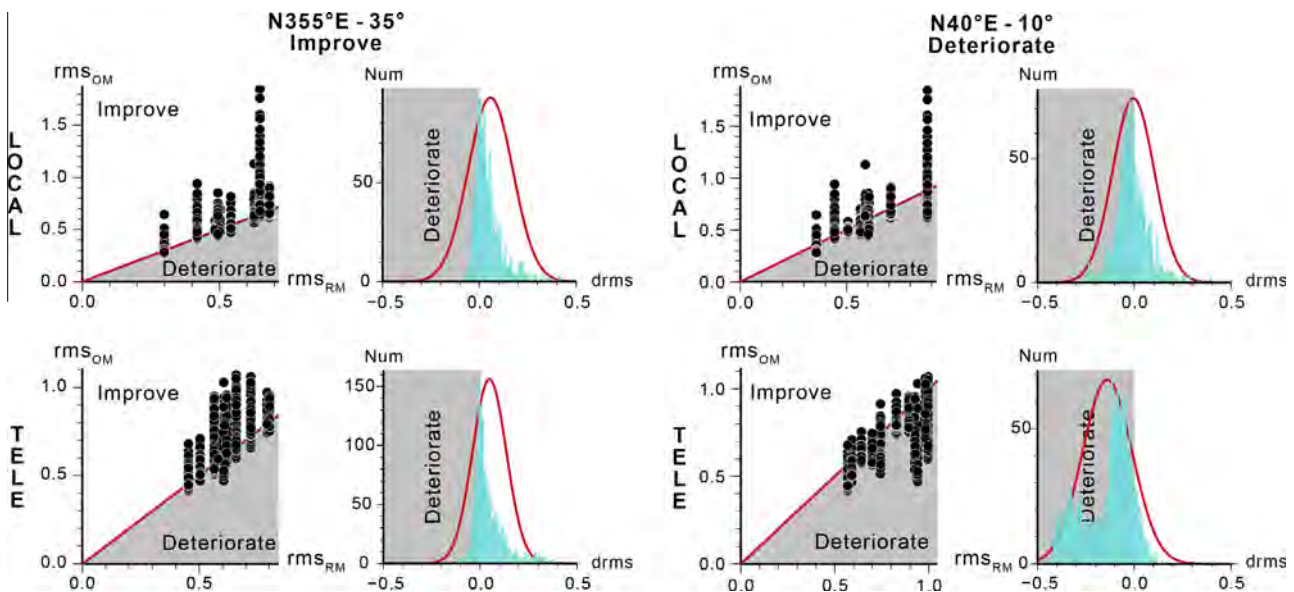


Fig. 6. Qualitative and quantitative views of the improvement/deterioration induced by one model compared to all models. The two planes (strike-dip = N40°E/10° and N355°E/35°) illustrate the difference between improvement (N355°E/35°) and deterioration (N40°E/10°) of relative waveform misfit. Indeed, plane N40°E/10° (left side) shows station misfits in the deterioration panel while plane N355°E/35° (right side) provides misfits in the improvement domain. rms_{Mtot} : rms of all models. rms_{Mtest} : model tested as reference model (i.e. N40°E/10° in the left side and N355°E/35° in the right side). Red line: line of equal rms ($rms_{Mtot} = rms_{Mtest}$). Black dots: station misfits (rms). Blue histogram: histogram of the repartition of the difference in rms (dms) between the model of reference and the other geometries. Red curve: Gaussian curve computed from the repartition of dms . (For interpretation of the references to colour in this figure legend, the reader is referred to the web version of this article.)

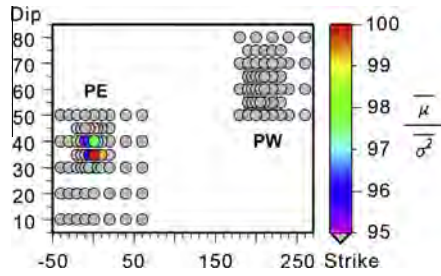


Fig. 7. Results of the statistical approach on the repartition of *drms*. Results are plotted in map of dip as a function of strike. Colored circles are results with $\frac{\bar{\mu}}{\bar{\sigma}^2} \geq 95\%$. When the ratio is lower than 95%, circles are gray. *PE* and *PW* are abbreviations for planes that dip eastward and westward respectively.

a mean situated mainly in the improvement domain and a pulse shape (i.e. positive and high μ for a low σ^2) in both datasets. In more practical ways, we look for results with high $\frac{\bar{\mu}}{\bar{\sigma}^2}$ (in percentage), where $\bar{\mu}$ and $\bar{\sigma}^2$ are the average of μ and σ^2 over the two datasets. This ratio is set to vary between 100% for the highest $\frac{\bar{\mu}}{\bar{\sigma}^2}$ (the best solution) and 0% for the lowest one. For an easy comparison with focal mechanism best fit dip-strike graph of Fig. 4, only results with $\frac{\bar{\mu}}{\bar{\sigma}^2}$ above 95% are shown with color circles in Fig. 7 (gray circles correspond to solutions with a ratio lower than 95%). Solutions that deteriorate the best difference in rms (*drms*) less than 5% ($\frac{\bar{\mu}}{\bar{\sigma}^2} \geq 95\%$) are located in the domain of plane *PE* with a best solution for the geometry N000°E/35° (strike/dip). Only two other solutions deteriorate the best one less than 2%: N010°E/35° at 1% ($\frac{\bar{\mu}}{\bar{\sigma}^2} = 99\%$) and N005°E/40° at 2% ($\frac{\bar{\mu}}{\bar{\sigma}^2} = 98\%$). If we compare with results obtained from the average rms (Fig. 5), best results are identical except for the dip that is slightly shallower with the statistical method. However, for solutions at 2% from the best one, the statistical method successfully restrict the number of possible geometry to the above three planes (compared to the twenties of possible geometries determined by the average approach).

4.4. Selection of the best geometry

To select which geometry is the appropriate one, we compare waveform adjustment from both datasets obtained from the above three geometries of *PE* (N000°E/35°, N010°E/35° and N005°E/40°) and from the best solution of *PW* (N210°E/60°, ($\frac{\bar{\mu}}{\bar{\sigma}^2} = 87.5\%$)).

Local waveforms are globally well modeled (Fig. 8), however, the planes N005°E/40° and N210°E/60° fail to recover the first arrival polarity (red exclamation marks in Fig. 8) on the Z component of station T047 in the case of N005°E/40° and the East component of station T002 for N210°E/60°. Those two stations are interestingly located either in the strike direction of nodal plane (for T002) or in the direction perpendicular to them (T047, Fig. 2b). Therefore, they are extremely sensitive to small variations of geometry leading to a polarity of the first arrival only recovered by models that closely approach the real fault plane geometry. Hence, planes N005°E/40° and N210°E/60° are excluded from being the actual fault plane. The two remaining planes are both located in the *PE* domain with N000°E/35° providing a slightly better waveform adjustment (black stars on Fig. 8) than N010°E/35° and is consequently favored by local strong motion data as the fault plane.

Concerning teleseismic data (Fig. 9), few differences in waveform adjustment can be seen among the four possible geometries. The earthquake magnitude seems to be too low for those data to discriminate strongly the fault plane from the nodal plane or small variations of solutions inside the *PE* domain. As a result, the solution determined by local data with a plane striking at N000°E and dipping 35° eastward is the geometry we select for the T2 earthquake.

5. Details on the coseismic fault slip

Before describing the coseismic fault slip behavior of T2, we first analyze deviations on the inversion free parameters.

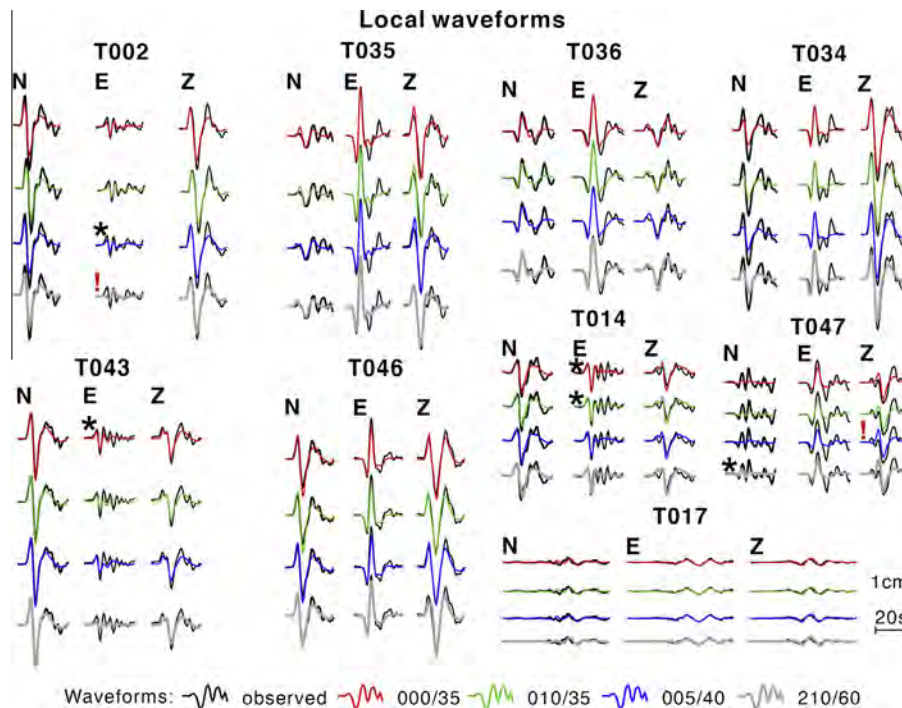


Fig. 8. Local strong motion waveform adjustment. All waveforms are plotted with the same horizontal and vertical scale. Observed waveforms are in black to compare with compute one: N000°E/35° (in red), N010°E/35° (in green) and N005°E/40° (in blue) for the *PE* domain, and N210°E/60° (in gray) for the *PW* set. Red exclamation marks indicate a computed waveform with a wrong polarity of the first arrival. Black stars signal the best waveform adjustment. (For interpretation of the references to colour in this figure legend, the reader is referred to the web version of this article.)

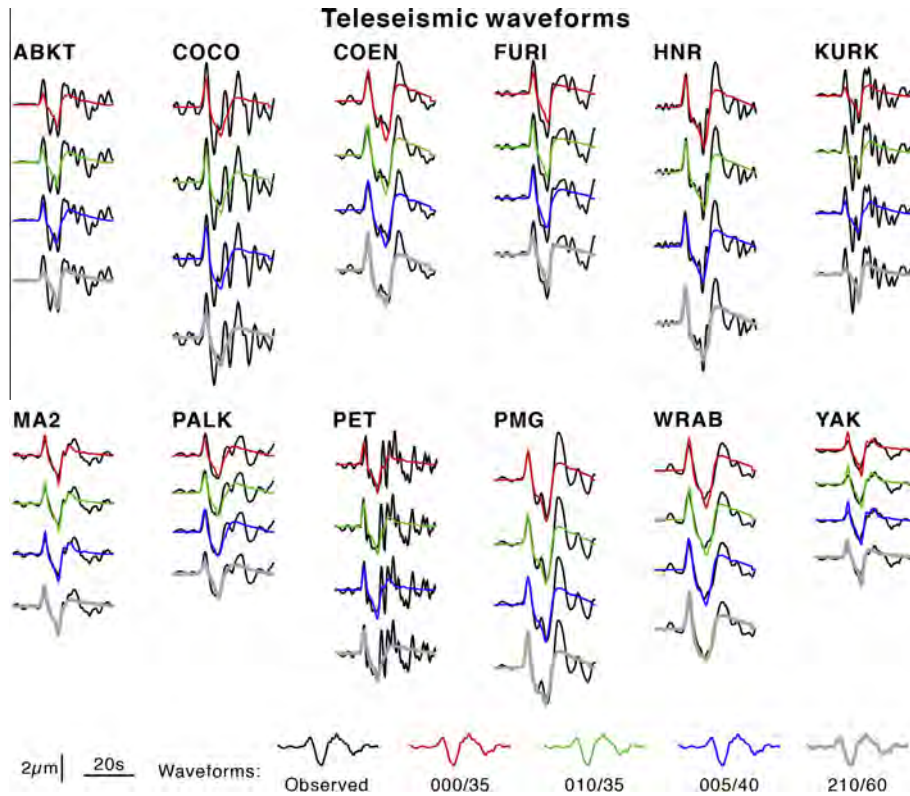


Fig. 9. Telesismic waveform adjustment. The same legend as in Fig. 8 is used. All waveforms are plotted with an identical horizontal and vertical scale.

5.1. Uncertainties on free parameters

Since we conducted a non-linear inversion by using a simulated annealing algorithm to retrieve the slip, rake and rupture time of each subfault of our model, a wide range of fault slip distributions is tested before converging toward the best result. It is then possible to compute the deviation (σ) on all free parameters over all tested slip distributions (Mozziconacci et al., 2009, 2013):

$$\sigma = \sqrt{\frac{\sum_1^{nmod} \frac{(m_{ij} - m_i)}{E_j}}{\sum_1^{nmod} \frac{1}{E_j}}} \quad (2)$$

with

$$E_j = \frac{\sum_1^2 P f}{\sum_1^2 P} + f_{M_0} + f_s \quad (3)$$

In the expression of σ (Eq. (2)), m_i is the i th parameter of the best fault slip distribution, m_{ij} and E_j are the respective i th parameter and the cost function of the j th fault slip distribution, and $nmod$ is the total number of slip distribution tested by the inversion. In E_j (Eq. (3)), P is the weight on the data set, f the misfit between observed and computed waveform, f_{M_0} , the minimizing function of the total moment magnitude and the smoothing function on the slip distribution. For the T2 earthquake, we considered equally local and telesismic data ($P_{local} = P_{telesismic} = 1$).

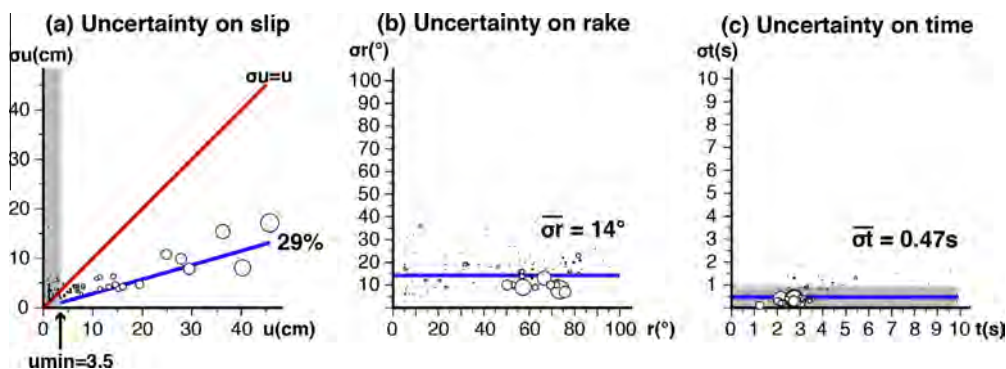


Fig. 10. Deviation and uncertainties on the free parameters. (a) Uncertainty on slip. In the graph of slip deviation (σu) as a function of slip (u), when u is larger than 3.5 cm (u_{min}), u is constrained ($\sigma u < u$), and a linear relationship develops between σu and u with a slope of 29%. Gray rectangle: domain in which u is not constrained ($\sigma u > u$). Red line: linear relationship between σu and u of equation $\sigma u = 0.29 u$. White circles diameters is function of u . The same diameter scale for white circles is used in (b) and (c). (b) Uncertainty on rake. In the graph of rake deviation (σr) as a function of rake (r), for subfaults with $u \geq u_{min}$, deviations stabilize at 14° ($\bar{\sigma r}$). Blue line: uncertainty on rake ($\bar{\sigma r}$). (c) Uncertainty on time. As for the rake, in the graph of time deviation (σt) as a function of time (t), for subfaults with $u \geq u_{min}$ deviations stabilize at 0.47 s ($\bar{\sigma t}$). Blue line: uncertainty on time ($\bar{\sigma t}$). Gray rectangle: domain for which $\sigma t \leq 2 * \sigma t$. (For interpretation of the references to colour in this figure legend, the reader is referred to the web version of this article.)

From the graph of the standard deviation on slip (σu) as function of the slip (u , Fig. 10), we evaluated the minimum slip (u_{min}) above which the slip is well constrained ($\sigma u < u$). Above u_{min} a linear relationship develops between u and σu with a slope viewed as the uncertainty on slip. For subfaults with a slip larger than u_{min} , deviations on rake (σr) and time (σt) stabilize around mean values taken as rake and time uncertainties ($\bar{\sigma r}$ and $\bar{\sigma t}$ respectively). Consequently, subfaults with slip larger than the critical slip u_{min} have their free parameters well constrained (Mozziconacci et al., 2013).

In Fig. 10, we plotted deviations on the free parameters (slip, rake and time) for our best model (N000°E/35°). From deviations on slip (σu , Fig. 10a), u_{min} is evaluated at 3.5 cm. Above u_{min} , slip is constrained at 29% and uncertainties on rake ($\bar{\sigma r}$) and time ($\bar{\sigma t}$) are 14° and 0.47 s respectively (Fig. 10b and c).

5.2. Rupture velocity and rupture propagation

Rupture velocity (Vr) is computed for subfaults that fulfill two conditions: (1) $u \geq u_{min}$ and (2) $\sigma t \leq 2 * \bar{\sigma t}$. For each subfault, we determined its rupture velocity from the ratio of its distance to the hypocenter (in km) and its time delay (in s). The average rupture velocity (Vr) is the average of subfaults rupture velocities (Vr_k) weighted by subfaults slip (u_k):

$$Vr = \frac{\sum_1^n u_k Vr_k}{\sum_1^n u_k} \quad (4)$$

As for free parameters, rupture velocity deviation (σVr) can be computed:

$$\sigma Vr = \sqrt{\frac{\sum_1^n u_k (Vr_k - Vr)^2}{\sum_1^n u_k}} \quad (5)$$

Since Vr is a unique value, σVr is both the deviation and the uncertainty (Mozziconacci et al., 2013).

The average Vr is estimated at 2.0 ± 0.6 km/s (Fig. 11a). However, on map view (Fig. 11b), Vr increases with the distance to the hypocenter, i.e., the rupture accelerates from 1.0 km/s near the hypocenter to 3.0 km/s at the edge of the final rupture area before to cease abruptly.

The slip distribution on the fault plane (Fig. 11c) and snapshots of the rupture propagation (Fig. 12) reveals that the rupture propagated circularly around the hypocenter with an oblique movement mainly reverse with a minor but significant left-lateral component. An average slip of 20 cm was determined for this earthquake with a maximum of 46 ± 13 cm leading to a moment magnitude M_w recomputed at 5.9. The rupture process lasted about 7 s with a main moment rate release between 2 and 5 s after the rupture began (Fig. 11d).

7. Discussion and conclusion

In summary, in order to retrieve the fault plane geometry of the second mainshock of the 2006 Taitung sequence, we used a

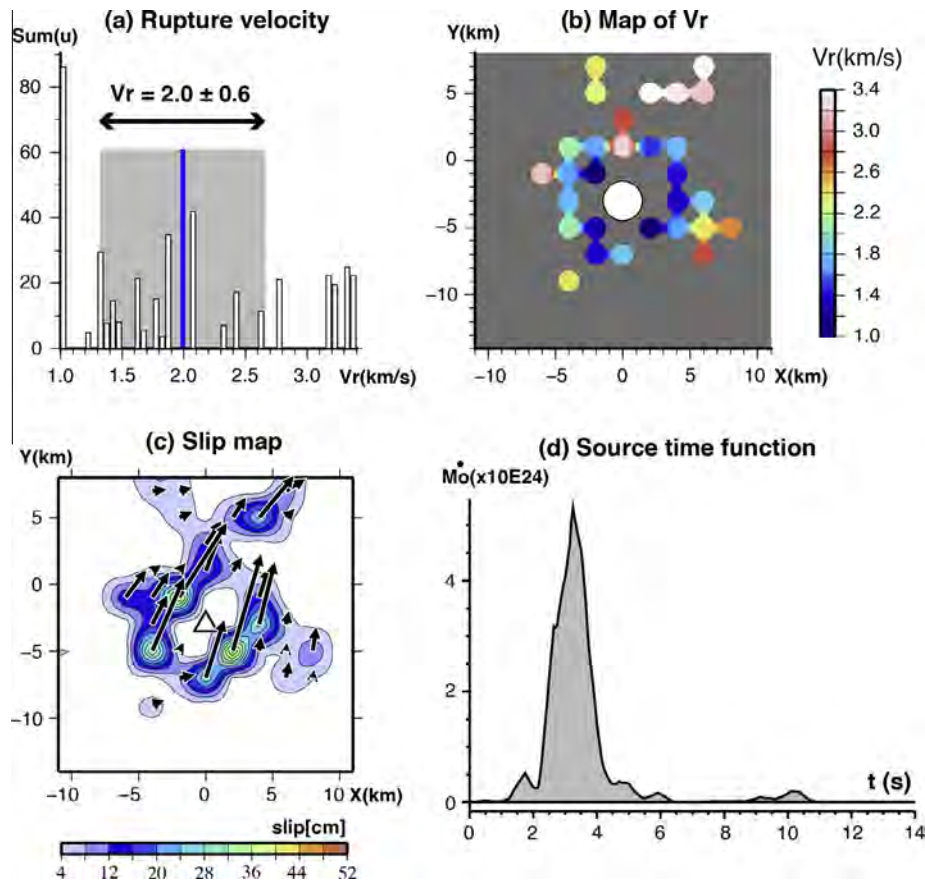


Fig. 11. Slip map and rupture velocity. (a) Graph of the amount of slip as function of Vr . Blue line: average rupture velocity. Gray rectangle: domain for which $Vr = 2.0 \pm 0.6$ km/s. (b) Map on Vr . Color scale is function of Vr and vary from 1.0 to 3.4 km/s (bounding values for Vr determination). Only subfaults that fulfill (1) $u \geq u_{min}$ and (2) $\sigma t \leq 2 * \bar{\sigma t}$ are plotted. (c) Slip map. Color scale is function of slip. To simplify the color scale values, the minimum color value is set at 4.0 cm rather than 3.5 cm (u_{min}). Black arrows point in the subfault rake direction and their size depend on the subfault slip. (d) Source time function. In the graph of the moment rate release (M_0) as a function of time (t), a single pulse of M_0 is observed mainly between 2 and 5 s after the rupture started. (For interpretation of the references to colour in this figure legend, the reader is referred to the web version of this article.)

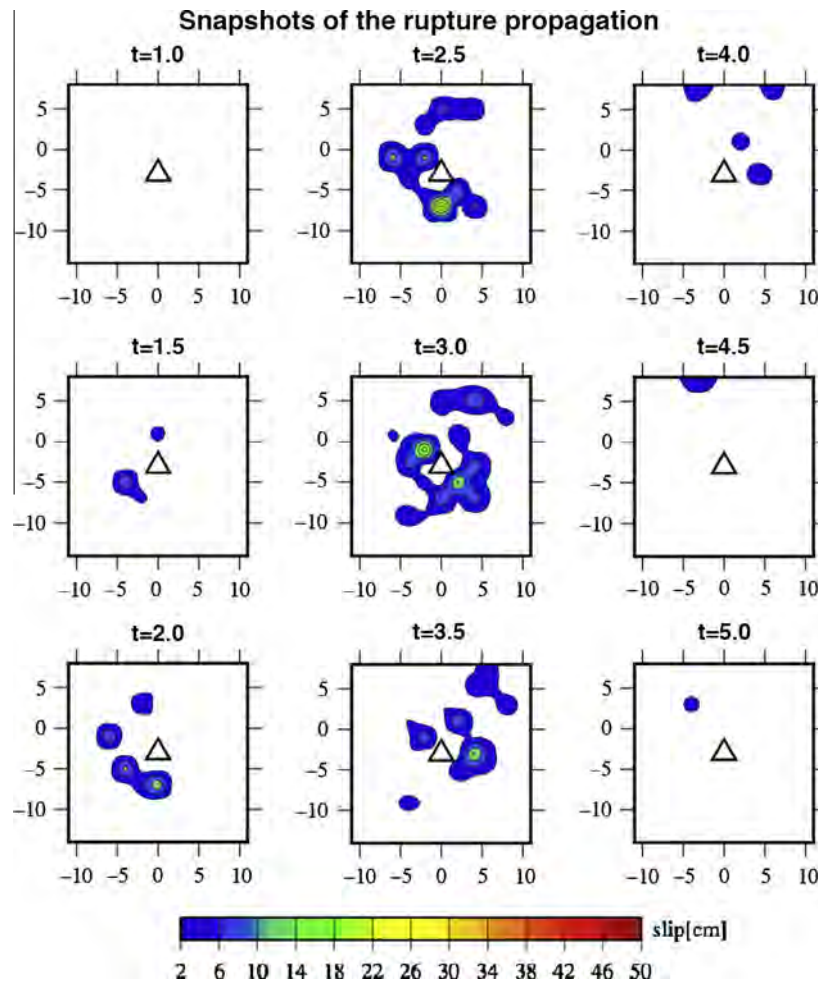


Fig. 12. Snapshots of the T2 earthquake rupture propagation. Black triangle: hypocenter. Above each slip map, the time (t) of the beginning of the snapshot (that all last 0.5 s) is indicated.

two-step approach. In the first step, we determined the focal mechanism of the event from two datasets of time-series issued from stations located at both local and teleseismic distances. Both datasets converge toward the same reverse focal mechanism, which is in good agreement with solutions provided by local (BATS) and teleseismic networks (GCMT, USGS). From this grid search, we restricted the number of possible geometries around the two nodal planes of the same focal mechanism. In the second step, we directly computed the fault slip displacement for the two sets of planes before converging toward the best solution in term of waveform adjustment. The usual approach of considering the average waveform misfit successes to discriminate the fault plane from the auxiliary one but fails to identify a precise fault geometry leading us to use a different approach. For that purpose, we considered a more statistical method on the repartition of difference in waveform misfit between models that successfully restrict the number of possible geometry. We obtained a best result striking a $N000^{\circ}E$ and dipping 35° eastward. For this geometry, the minimum of slip (u_{min}) the model can constrain is 3.5 cm. For subfaults with slip larger than this critical value (u_{min}), uncertainties on slip, rake and time are respectively 29%, 14° and 0.47 s. On this fault plane, the rupture accelerated while it propagated from the hypocenter (from 1.0 km/s to 3.0 km/s). The coseismic slip is confined within an area of about 16 km wide and 17 km long on the fault plane. The fault movement (rake) was oblique, mainly reverse with a non-negligible left-lateral component. On

average, a slip of 20 cm was determined with a maximum of 46 ± 13 cm giving a moment magnitude ($M_W = 5.9$) slightly lower than the local magnitude ($M_L = 6.0$).

T2 earthquake initiated in a very low slip area and propagated circularly. This nucleation feature seems to be a common characteristic in finite source rupture model (Mai et al., 2005). In the case of T2, subfaults with the highest slip (and low rupture velocity, Fig. 11) surround the area of low slip, leading to a straightforward estimation of this radius of 3 km. This low slip at the hypocenter results in a weak initiation of the source time function (Fig. 11d) with a delay of 1 s between the earthquake origin time and the start of non-negligible moment release. We tested the influence of velocity models on the low slip zone and the time delay by performing an inversion with only half-spaces for local station. It appears that velocity model have no influence on the low slip zone (its location and size) but tend to decrease the time delay. Consequently, the low slip zone and the time delay are not artifact but two characteristics of the T2 earthquake. If we consider a total source emission of 6 s, then the time delay corresponds to 1/6 of the total rupture process. Those characteristics (i.e. time delay and rupture initiation in a very low slip zone) are similar to the pre-slip model of Ellsworth and Beroza (1995). In their model, failure initiates aseismically with an episode of slow and stable sliding that gradually accelerates until the slipping zone reaches a critical size (called “nucleation zone”) after what the rupture process propagates seismically. When the

nucleation zone is observed, the nucleation phase last about 1/6 of the total source process (Ellsworth and Beroza, 1995, 1998) similar to what we obtained with the T2 earthquake. Comparing with the first mainshock of the Taitung 2006 sequence (T1), the rupture also initiated in a very low slip area of radius between 2 and 6 km and lasting about 2 s for a total source process of about 14 s (Mozziconacci et al., 2013), although the two faults belonging to different system. Whether these nucleation characteristics are common for moderate earthquakes in this area or restricted on some specific part of faults (for example fault

termination or bend) required further investigation. In this regard, we intend to analyze more events in a later study concerning the relationship between 2006 Taitung sequence and the 2003 Chengkung earthquake (M_w 6.8).

As mentioned before, in map view the aftershocks of the T2 earthquake distribute in a direction oblique to the main structure of the study area. However, on the 3D view (Fig. 13a) events are mostly contained inside the fault model of T2. In addition, they spread out between patches of relatively high coseismic slip releasing stress in areas that did not move significantly during

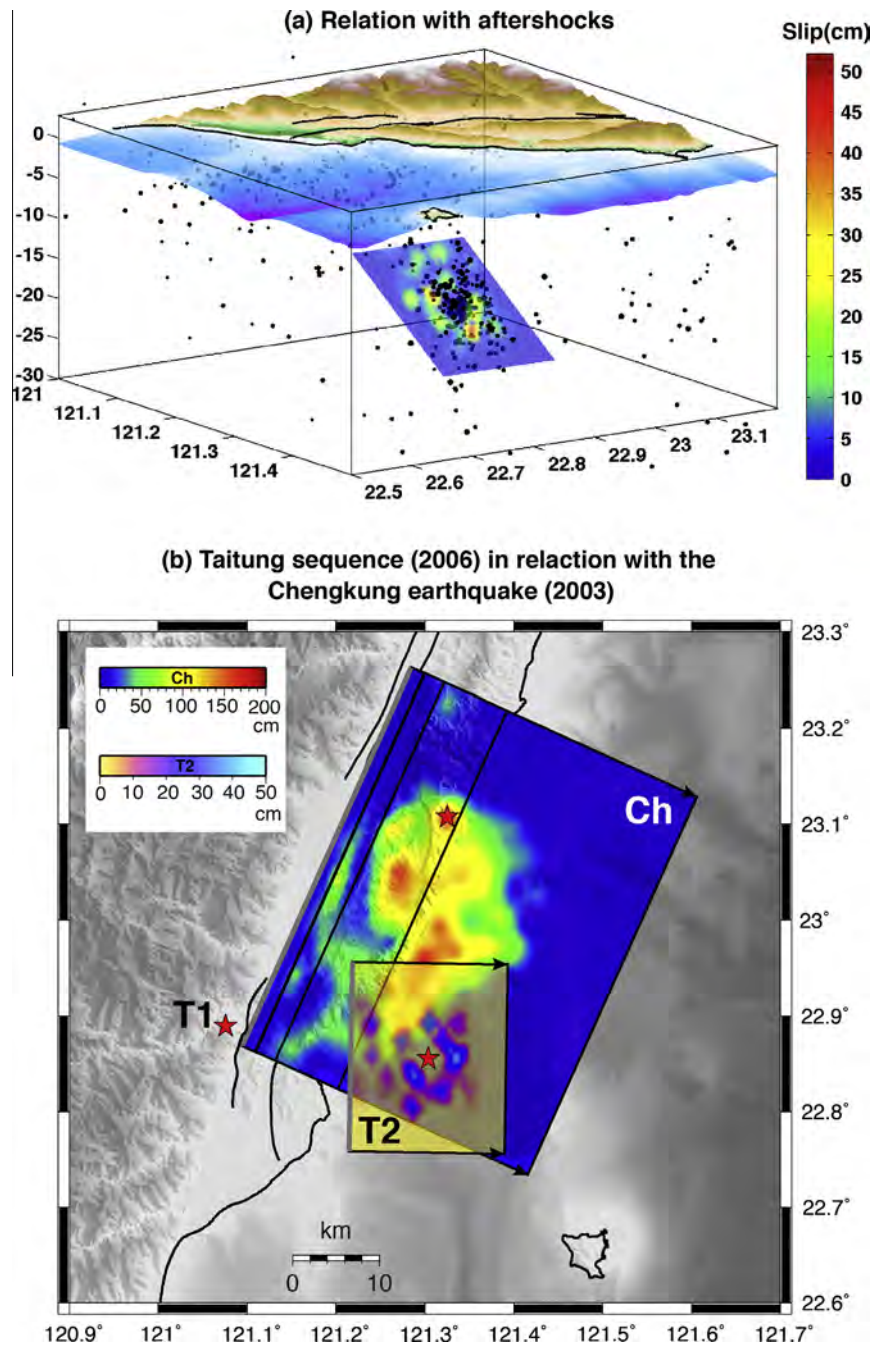


Fig. 13. Details on the coseismic fault slip distribution on T2. (a) Relation with aftershocks. On the 3D view, most of aftershocks (black dots) are clearly located inside the fault model and between the main slip patches of the mainshock slip map. Black lines: main faults. (b) Relation between T2 and the 2003 Chengkung earthquake (M_w 6.8). The slip distribution of T2 is superimposed with the slip distribution of the Chengkung earthquake (Ch) issued from Mozziconacci et al. (2009). Red stars: epicenter of the 2 mainshocks of the 2006 April sequence (T1 and T2) and of the Chengkung earthquake (Ch). Black lines: segments boundary of fault models. Gray line: shallowest portion of the fault model. Black arrows point in the dip direction. (For interpretation of the references to colour in this figure legend, the reader is referred to the web version of this article.)

the coseismic rupture. The link between aftershocks and T2 fault plane is now more straightforward. In map view (Fig. 13b), the fault model seems to correspond to the down-dip extension of the southern end of the LVF. A dip of 35° for an hypocenter at 18 km depth is in good agreement with the LVF geometry recovered from background microseismicity (Chen and Rau, 2002; Kuo-chen et al., 2004; Lee et al., 2003) and aftershocks alignments produced by the 2003 Chengkung earthquake (Kuo-chen et al., 2007; Lee et al., 2006). T2 also displays an oblique faulting (reverse and left-lateral) comparable to the LVF type of rupture. The Longitudinal Valley Fault is for those two reasons (geometry and fault movement) a good candidate for the T2 earthquake. Another point that comforts the LVF as the generative structure of T2 is the close spatial relationship between the 2003 Chengkung earthquake and T2 (Fig. 13b). The rupture of the latter is largely contained inside the southern part of the deeper segment of the Chengkung earthquake fault model. This segment has a dip similar to the T2 fault model (30° compared to 35° for T2) and lays in the same depth range (Mozziconacci et al., 2009). Moreover, rupture patches of T2 are located next to the edge of the Chengkung earthquake rupture area, bringing T2 in a position of aftershocks of this large earthquake (M_w 6.8) even those two events were separated by 2.5 years. Consequently, the LVF should be the fault that generated the T2 earthquake. If now we consider that T2 effectively activated the deepest segment of the LVF, the abrupt stop of the rupture while the propagation front accelerated could be explained by the fact that the rupture reached the main slip zone of the Chengkung earthquake (area that already slipped a few years earlier) and by the kink of the fault geometry. Indeed, after propagating circularly T2 ruptured upward until to reach the bending of the fault marking the junction between the deepest segment (dip = 30°) and the intermediate-shallower one (dip = 45–60°), the bending acting as a barrier on the rupture propagation.

In conclusion, the joint inversion of local strong motion and teleseismic waveforms provide new details on the Taitung earthquake sequence that struck the southern-end portion of the Longitudinal Valley in April 2006 with two major events (Fig. 13). The first event was located west to the LV and was the first moderate-large event (M_w = 6.1) ever recorded on the Central Range Fault during the last 30 years. Fourteen days later, the seismic activity migrated eastward on the main plate boundary fault, the LVF, with a mainshock of M_w 5.9. How the deformation was transmitted from the CRF to the LVF and if the 2006 Chengkung earthquake (M_w 6.8, that activated the LVF 2.5 years earlier) triggered this sequence despite the time delay are questions we want to address in the near future.

Acknowledgments

We would like to dedicate this paper to Prof. J. Angelier, who initiate the study on the first event of the Taitung sequence. We also thank W.C. Yu and T.-Y. Chang for valuable discussions. This research was supported by the Institute of Earth Sciences, Academia Sinica, and the ORCHID (Ministère des affaires étrangères) and LIA (INSU – CNRS – NSC) projects and was supported by the NSC grant number 101-2116-M-001-032.

Appendix A. Supplementary material

Supplementary data associated with this article can be found, in the online version, at <http://dx.doi.org/10.1016/j.jseae.2013.07.025>.

References

- Angelier, J., 1984. Geodynamics of the Eurasia-Philippine Sea Plate boundary. In: Colloquium on the Geodynamics of the Eurasian-Philippine Sea Boundary. Elsevier, Taiwan, ROC.
- Angelier, J., Chu, H., Lee, J., 1997. Shear concentration in a collision zone: kinematics of the Chihshang Fault as revealed by outcrop-scale quantification of active faulting, Longitudinal Valley, eastern Taiwan. *Tectonophysics* 274(1), 117–143. <[http://dx.doi.org/10.1016/S0040-1951\(96\)00301-0](http://dx.doi.org/10.1016/S0040-1951(96)00301-0)>.
- Angelier, J., Chu, H., Lee, J., Hu, J., 2000. Active faulting and earthquake hazard: the case study of the Chihshang fault, Taiwan. *J. Geodynam.* 29(3), 151–185. <[http://dx.doi.org/10.1016/S0264-3707\(99\)00045-9](http://dx.doi.org/10.1016/S0264-3707(99)00045-9)>.
- Barrier, E., 1985. Etude sismotectonique d'un grand accident actif: la Vallée Longitudinal de Taiwan (Taiwan, République de Chine). *Rev. Géol. Dynam. Géog. Phys.* 25, 45–60.
- Barrier, E., Angelier, J., 1986. Active collision in eastern Taiwan: the Coastal Range. *Tectonophysics* 125(1), 39–72. <[http://dx.doi.org/10.1016/0040-1951\(86\)90006-5](http://dx.doi.org/10.1016/0040-1951(86)90006-5)>.
- BATS. Broadband Array in Taiwan for Seismology. (accessed June 2013). <<http://tecws.earth.sinica.edu.tw/BATS/>>.
- Biq, C., 1965. The east Taiwan rift. *Petroleum Geol. Taiwan* 4, 93–106.
- Biq, C., 1972. Dual trench suture in Taiwan-Luzon region. *Proc. Geol. Soc. China* 15, 65–75.
- Bouchon, M., 1981. A simple method to calculate Green's functions for elastic layered media. *Bull. Seismol. Soc. Am.* 71 (4), 959–971.
- Chai, B., 1972. Structure and tectonic evolution of Taiwan. *Am. J. Sci.* 272(5), 389–422. <<http://dx.doi.org/10.2475/ajs.272.5.389>>.
- Chen, H., Rau, R., 2002. Earthquake locations and style of faulting in an active arc-continent plate boundary: the Chihshang fault of eastern Taiwan. In: AGU Fall Meeting Abstracts, San Francisco, pp. 1277.
- Chen, H., Hsu, Y., Lee, J., Yu, S., Kuo, L., et al., 2009. Coseismic displacements and slip distribution from GPS and leveling observations for the 2006 Peinan earthquake (M_w 6.1) in southeastern Taiwan. *Earth Planets Space* 61 (3), 299–318.
- Crespi, J., 1996. Deformation partitioning at shallow crustal levels in the Taiwan arc-continent collision zone. *J. Geol. Soc. China* 39 (2), 143–150.
- CWB. Central Weather Bureau. (accessed June 2013). <<http://www.cwb.gov.tw/eng/>>.
- Delouis, B., submitted for publication. FMNEAR: determination of focal mechanism and first estimate of rupture directivity using near source records and a linear distribution of point sources. *Bullet. Seismol. Soc. Am.*
- Delouis, B., Legrand, D., 1999. Focal mechanism determination and identification of the fault plane of earthquakes using only one or two near-source seismic recordings. *Bull. Seismol. Soc. Am.* 89 (6), 1558–1574.
- Delouis, B., Giardini, D., Lundgren, P., Salichon, J., 2002. Joint inversion of InSAR, GPS, teleseismic, and strong-motion data for the spatial and temporal distribution of earthquake slip: application for the 1999 Izmit mainshock. *Bullet. Seismol. Soc. Am.* 92(1), 278–299. <<http://dx.doi.org/10.1785/0120000806>>.
- Delouis, B., Charley, J., Vallée, M., 2008. Fast determination of earthquake source parameters from strong motion records: MW, focal mechanism and slip distribution. In: EGU General Assembly, Geophys. Res. Abstr. Vienna (Austria). Abstract 04939.
- Ellsworth, W., Beroza, G., 1995. Seismic evidence for an earthquake nucleation phase. *Science* 268(5212), 851–855. <<http://dx.doi.org/10.1126/science.268.5212.851>>.
- Ellsworth, W., Beroza, G., 1998. Observation of the seismic nucleation phase in the Ridgecrest, California, earthquake sequence. *Geophys. Res. Lett.* 25, 401–404. <<http://dx.doi.org/10.1029/97GL53700>>.
- GCMT. Global Moment Tensor Project. (accessed June 2013). <<http://earthquake.usgs.gov/earthquakes/eqarchives/sopar/>>.
- Ho, C., 1982. Tectonic Evolution of Taiwan: Explanatory Text of the Tectonic Map of Taiwan. Ministry of Economic Affairs, Republic of China.
- Ho, C., 1986. A synthesis of the geologic evolution of Taiwan. *Tectonophysics* 125(1–3), 1–16. <[http://dx.doi.org/10.1016/0040-1951\(86\)90004-1](http://dx.doi.org/10.1016/0040-1951(86)90004-1)>.
- Ihmlé, P., Ruegg, J., 1997. Source tomography by simulated annealing using broadband surface waves and geodetic data: application of the $M_w=8.1$ Chile 1995 event. *J. Int.* 131(1), 146–158. <<http://dx.doi.org/10.1111/j.1365-246X.1997.tb00601.x>>.
- IRIS. Incorporated Research Institution for Seismology (IRIS) consortium Data Management Center (DMC). (accessed November 2011). <<http://www.iris.edu>>.
- Kirkpatrick, S., Gelatt, J., Vecchi, M., 1983. Optimization by simulated annealing. *Science* 220(4598), 671–680. <<http://dx.doi.org/10.1126/science.220.4598.671>>.
- Kuo-chen, H., Wu, Y., Chang, C., Hu, J., Chen, W., 2004. Relocation of eastern Taiwan earthquakes and tectonic implications. *Terrestrial, Atmospheric Oceanic Sci.* 15, 647–666.
- Kuo-chen, H., Wu, Y., Chen, Y., Chen, R., 2007. 2003 M_w = 6.8 Chengkung earthquake and its related seismogenic structures. *J. Asian Earth Sci.* 31(3), 332–339. <<http://dx.doi.org/10.1016/j.jseae.2006.07.028>>.
- Lallemant, S., Font, Y., Bijwaard, H., Kao, H., 2001. New insights on 3-D plates interaction near Taiwan from tomography and tectonic implications. *Tectonophysics* 335, 229–253. <[http://dx.doi.org/10.1016/S0040-1951\(01\)00071-3](http://dx.doi.org/10.1016/S0040-1951(01)00071-3)>.
- Lee, J., Angelier, J., Chu, H., Yu, S., Hu, J., 1998. Plate-boundary strain partitioning along the sinistral collision suture of the Philippine and Eurasian plates: analysis of geodetic data and geological observation in southeastern Taiwan. *Tectonics* 17(6), 859–871. <<http://dx.doi.org/10.1029/98TC02205>>.

- Lee, J., Angelier, J., Chu, H., Hu, J., Jeng, F., 2001. Continuous monitoring of an active fault in a plate suture zone: a creepmeter study of the Chihshang Fault, eastern Taiwan. *Tectonophysics* 333(1–2), 219–240. <[http://dx.doi.org/10.1016/S0040-1951\(00\)00276-6](http://dx.doi.org/10.1016/S0040-1951(00)00276-6)>.
- Lee, J., Angelier, J., Chu, H., Jeng, F., Rau, R., 2003. Active fault creep variations at Chihshang, Taiwan, revealed by creepmeter monitoring, 1998–2001. *J. Geophys. Res.* 108(B11), 2528. <<http://dx.doi.org/10.1029/2003JB002394>>.
- Lee, J., Chu, H., Angelier, J., Hu, J., Chen, H., Yu, S., 2006. Quantitative analysis of surface coseismic faulting and postseismic creep accompanying the 2003, $M_W = 6.5$, Chengkung earthquake in eastern Taiwan. *J. Geophys. Res.* 111(B2), B02405. <<http://dx.doi.org/10.1029/2005JB003612>>.
- Lundgren, P., Protti, M., Donnellan, A., Heflin, M., Hernandez, E., Jefferson, D., 1999. Seismic cycle and plate margin deformation in Costa Rica - GPS observations from 1994 to 1997. *J. Geophys. Res.* 104(B12), 28915–28926. <<http://dx.doi.org/10.1029/1999JB900283>>.
- Mai, P., Spudich, P., Boatwright, J., 2005. Hypocenter locations in finite-source rupture models. *Bullet. Seismol. Soc. Am.* 95(3), 965–980. <<http://dx.doi.org/10.1785/0120040111>>.
- Malavieille, J., Lallemand, S., Dominguez, S., Deschamps, A., Lu, C., Schnurle, P., ACT (Active Collision in Taiwan) Scientific Crew (2002). Arc-continent collision in Taiwan: new marine observations and tectonic evolution. In: Byrne, T.B., Liu, C.S. (Eds.), *Geology and Geophysics of an Arc-continent Collision*, Taiwan, Republic of China, Boulder, Colorado, Geological Society of America Special Paper, 358, pp. 187–211.
- Mozziconacci, L., Delouis, B., Angelier, J., Hu, J., Huang, B., 2009. Slip distribution on a thrust fault at a plate boundary: the 2003 Chengkung earthquake, Taiwan. *Geophys. J. Int.* 177(2), 609–623. <<http://dx.doi.org/10.1111/j.1365-246X.2009.04097.x>>.
- Mozziconacci, L., Delouis, B., Huang, B., Lee, J., Béthoux, N., 2013. Determining fault geometry from the distribution of coseismic fault slip related to the 2006 Taitung earthquake, eastern Taiwan. *Bullet. Seismol. Soc. Am.* 103(1), 394–411. <<http://dx.doi.org/10.1785/0120110232>>.
- Nábělek, J., 1984. Determination of Earthquake Source Parameters from Inversion of Body Waves, Ph.D. thesis, Massachusetts Institute of Technology.
- Olson, A., Aspel, R., 1982. Finite faults and inverse theory with applications to the 1979 Imperial Valley earthquake. *Bulletin of the Seismological Society of America* 72 (6A), 1969–2001.
- Shyu, J., Sieh, K., Chen, Y., Chung, L., 2006. Geomorphic analysis of the Central Range Fault, the second major active structure of the Longitudinal Valley suture, eastern Taiwan. *Geol. Soc. Am. Bulletin*. 118(11–12), 1447–1462. <<http://dx.doi.org/10.1130/B25905.1>>.
- Shyu, J., Sieh, K., Chen, Y., Chuang, R., Wang, Y., Chung, L., 2008. Geomorphology of the southernmost Longitudinal Valley fault: Implications for evolution of the active suture of eastern Taiwan. *Tectonics* 27(1), TC1019. <<http://dx.doi.org/10.1029/2006TC002060>>.
- Tsai, Y., 1986. Seismotectonics of Taiwan. *Tectonophysics* 125(1–3), 17–37. <[http://dx.doi.org/10.1016/0040-1951\(86\)90005-3](http://dx.doi.org/10.1016/0040-1951(86)90005-3)>.
- Tsai, Y., Hsiung, Y., Liaw, H., Lueng, H., Yao, T., Yeh, Y., Yeh, Y., 1974. A seismic refraction study of eastern Taiwan. *Petroleum Geol. Taiwan* 11 (165–182).
- USGS. U.S. Geological Survey. (accessed June 2013). <<http://earthquake.usgs.gov/earthquakes/eqarchives/sopar/>>.
- Wells, D., Coppersmith, K., 1994. New empirical relationships among magnitude, rupture length, rupture width, rupture area, and surface displacement. *Bull. Seismol. Soc. Am.* 84 (4), 974–1002.
- Wu, Y., Chen, Y., Chang, C., Chung, L., Teng, T., Wu, F., Wu, C., 2006. Seismogenic structure in a tectonic suture zone: with new constraints from 2006 M_W 6.1 Taitung earthquake. *Geophys. Res. Lett.* 33(22), L22305. <http://dx.doi.org/10.1029/2006GL027572>.
- Yu, S., Kuo, L., 2001. Present-day crustal motion along the Longitudinal Valley Fault, eastern Taiwan. *Tectonophysics* 333(1–2), 199–217. [http://dx.doi.org/10.1016/S0040-1951\(00\)00275-4](http://dx.doi.org/10.1016/S0040-1951(00)00275-4).